Nano Energy 32 (2017) 397–407

Contents lists available at ScienceDirect

Nano Energy

journal homepage: www.elsevier.com/locate/nanoen

Full paper

In situ analysis of SnO_2/Fe_2O_3/RGO to unravel the structural collapse mechanism and enhanced electrical conductivity for lithium-ion batteries

Kangsoo Lee[a,b], Seoyoon Shin[b], Thomas Degen[c], Wooyoung Lee[a,*], Young Soo Yoon[b,*]

[a] Department of Materials Science and Engineering, Yonsei University, Shinchon-dong, 262 Seongsanno, Seodaemoon-gu, Seoul 120-749, Republic of Korea
[b] Department of Chemical & Biological Engineering, Gachon University, Seongnamdaero 1342, 461-710 Gyeonggi-do, Republic of Korea
[c] PANalytical B.V., Lelyweg 1, 7603 EA Almelo, The Netherlands

ARTICLE INFO

Keywords:
Iron oxide
Tin oxide
Reduced graphene oxide
Nanoparticles
Anode
Li ion battery

ABSTRACT

Herein, we describe a microwave-assisted hydrothermal process to synthesize α-Fe_2O_3 nanotubes/SnO_2 nanorods/reduced graphene oxide (FNT/S/RGO) for application as a high-performance anode in lithium-ion batteries (LIBs). The composite products exhibit anisotropic growth because of heteronucleation and the preferred orientation of SnO_2. SnO_2 nanorods on the FNT surfaces are converted into Sn metal during the alloying/dealloying reaction, which offers improved electrical conductivity. The FNT/S/RGO show substantially enhanced electrochemical properties because of the reduced volume expansion effect, which improves the electrical and Li-ion conductivity and provides a large surface area. As a consequence, the FNT/S/RGO anode delivers a high reversible capacity of 883 mA h g^{-1} even at a current density of 200 mA g^{-1}, with a capacity retention of 90% between the 1st and 220th cycles, excellent high-rate capacity (382 mA h g^{-1} at 4320 mA g^{-1}), and long-term cycle durability (maintaining 629 mA h g^{-1} at 1000 mA g^{-1} for 1000 cycles). The presented FNT/S/RGO electrodes are the most efficient SnO_2- and Fe_2O_3-based anode electrodes reported thus far for LIBs. The origin of the synergistic effect and the reaction mechanism of the FNT/S/RGO was thoroughly investigated using various *in situ* transmission electron microscopy, electrochemical impedance spectroscopy, and X-ray diffraction analysis methods.

1. Introduction

Iron oxide and tin oxide are considered promising anode materials because of their high theoretical capacity (Fe_2O_3 and SnO_2: ~1005 and ~781 mA h g^{-1}), eco-friendly materials, and natural abundance, which can be much higher than that of a commercial graphite anode (372 mA h g^{-1}) [1,2]. However, one of the serious drawbacks of metal oxides, including Fe_2O_3 and SnO_2, for LIBs is their low electrical conductivity and severe volume expansion during the insertion and extraction of Li ions, which can result in the detachment of the metal oxide anode from the current collector. This issue is directly related to a large initial capacity drop, poor rate capability, and insufficient cycle performance [3]. Various groups have suggested solutions to these serious problems by designing structures such as nanorods, nanotubes, nanocubes, nanoparticles, 3d porous structures, hollow shells, and epitaxial growth structures; however, all these solutions provide unsatisfactory rate capacity and long-term cyclability [4–9].

Because the high rate capacity and long-term cyclability remain unsatisfactory, hollow nanostructures to prevent volume expansion and provide high rate capability for metal oxide anodes have attracted considerable interest because of their excellent resistance to volume expansion and short diffusion lengths for Li ions [10]. Nevertheless, one of the drawbacks of preparing hollow structures is the formation of a hard template during preprocessing, which is a tedious task because of the difficulty in obtaining a hollow nanostructure. The hard template from the hollow nanostructure is difficult to remove while keeping the hollow nanostructure intact. Synthesis without a template by calcination is favorable. Therefore, in this study, we investigate the hollow nanostructure of template-free α-Fe_2O_3 nanotubes/SnO_2/RGO (FNT/S/RGO) prepared using a microwave-assisted hydrothermal process to maximize the practical use and large-scale processability of Fe_2O_3 nanotubes and SnO_2 nanorods as anode materials for LIBs.

Recently, SnO_2–Fe_2O_3 composites have been reported to exhibit better cycling characteristics than pristine SnO_2 or Fe_2O_3 due to the presence of metallic components during conversion reaction [5,11]. However, the electrochemical performance of simply mixed SnO_2–Fe_2O_3 composites is unsatisfactory because of the huge volume changes and low electrical conductivity in SnO_2 and Fe_2O_3 during the reaction [5,8,12]. In the present work, the unique hybrid structure of FNT/S/RGO is proposed to overcome these drawbacks. To reduce the volume

* Corresponding authors.
E-mail addresses: wooyoung@yonsei.ac.kr (W. Lee), benedicto@gachon.ac.kr (Y.S. Yoon).

http://dx.doi.org/10.1016/j.nanoen.2016.12.058
Received 9 November 2016; Received in revised form 7 December 2016; Accepted 30 December 2016
Available online 31 December 2016

change, α-Fe_2O_3 nanotubes were fabricated with the free space of a hollow structure, which can offer superior and stable cyclability. The Fe_2O_3 and SnO_2 structure was synthesized as hollow α-Fe_2O_3 (wall thickness of ~20 nm) and SnO_2 nanorods (rod diameter of ~10 nm) to apply electric vehicle, hybrid electric vehicle and energy storage systems, which can provide high rate performance [12]. In addition, the RGO provides advantages such as improved electrical conductivity, a buffer effect, and a large surface area to accommodate Li ions [13,14]. Therefore, the synergistic improvement provided by RGO and FNT/S compared to pristine α-Fe_2O_3 and SnO_2 enables high capacity retention, enhanced rate capability, and good cycle durability.

The electrochemical performance of an anode, such as its cyclability, rate capability, and coulombic efficiency, are strongly related to the charge transfer and ion diffusion behavior at the electrode surface [15]. The formation of the solid electrolyte interface (SEI) on a complicated shape and the co-relationship between the collapse mechanism and the structural strain of the multi-metal oxide, which is generated from the shape, remain difficult to define. Recently, *in situ* TEM conducted using a bias-controlled *in situ* TEM holder revealed structural changes during lithiation; however, examining both the behavior of the decomposed electrolytes and the practical structural failure due to the use of a solid-type electrolyte or ionic liquid is difficult [16–18]. Therefore, FNT/S/RGO electrodes were characterized using stacked graphene sheets that contained a liquid electrolyte; the advantages of this approach are easy fabrication, applicability to any conventional transmission electron microscope, and similarity to a realistic measurement environment because of the liquid electrolyte [19,20]. Furthermore, the electrochemical characterization during cycling strongly affects the electron conductivity, conversion mechanism, and structural integrity. Therefore, various *in situ* analysis techniques (TEM, electrochemical impedance spectroscopy (EIS), and XRD) were used to examine the cycle mechanism of α-Fe_2O_3 and SnO_2. Profound insights of the reaction behavior and conversion mechanism of Fe_2O_3 nanotubes and SnO_2 nanorods were obtained.

2. Experimental section

2.1. Preparation of α-Fe_2O_3 nanotubes (FNTs)

All chemicals in this study were of analytical reagent grade. The FNTs were fabricated using a microwave-assisted hydrothermal process (MARS 6, CEM Co.). $FeCl_3{\cdot}6H_2O$, $NH_4H_2PO_4$, and Na_2SO_4 were mixed in 40 ml of deionized (DI) water, and the resulting solution was transferred to a Teflon vessel and heated at 220 °C for 30 min. After the synthesis was complete and the mixture was cooled to room temperature, the precipitate was centrifuged with DI water and dried in an

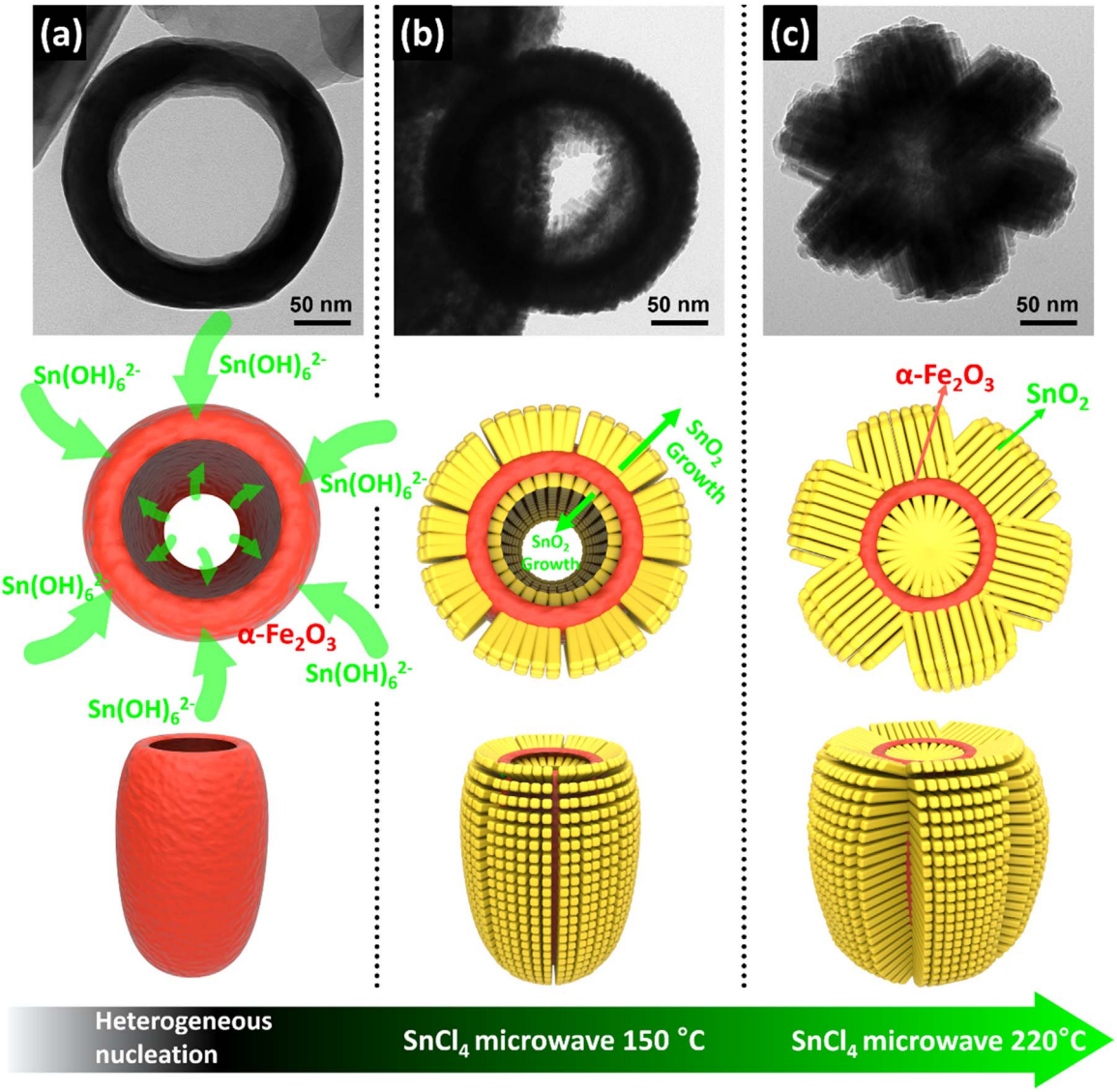

Fig. 1. TEM images and schematics of the microwave-assisted hydrothermal synthesis process of (a) FNT at 220 °C, (b) FNT/S at 150 °C, and (c) FNT/S at 220 °C.

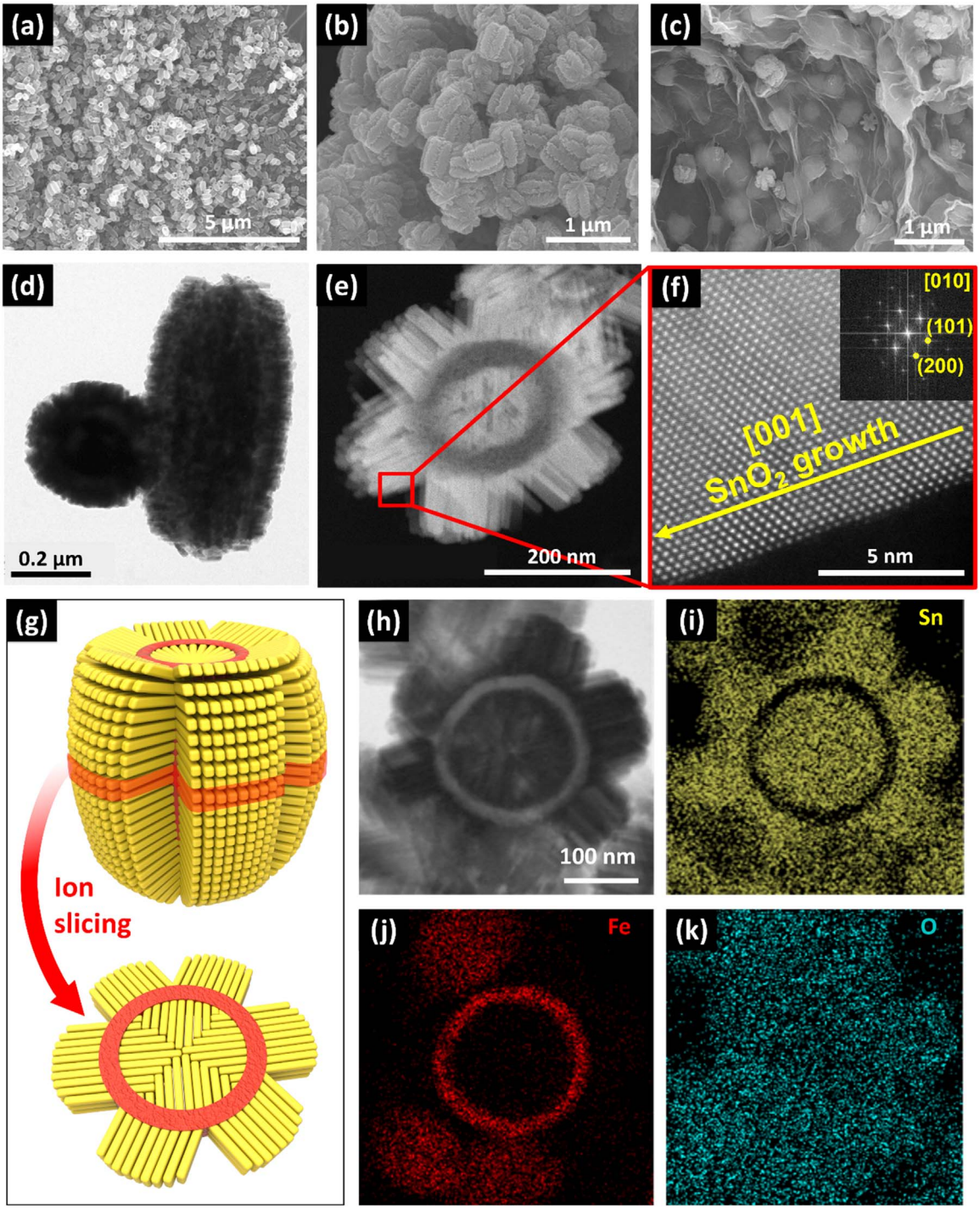

Fig. 2. SEM images of (a) FNT, (b) FNT/S, and (c) FNT/S/RGO, (d) TEM image of the top (left) and side view (right) of FNT/S, (e) dark-field TEM image of the ion-sliced FNT/S specimen, (f) high-resolution TEM image of SnO_2 nanorod of FNT/S/RGO (enlarged image of boxed area from (e)), and fast Fourier transform (FFT) analysis (inset), (g) schematic of the ion-slicing process of FNT/S for a TEM investigation of FNT/S/RGO, (h) TEM image of ion-sliced FNT/S/RGO, (i), (j), and (k) EDS mapping images of (h) for Sn, Fe and O, respectively.

electrical oven at 70 °C for 12 h.

2.2. Preparation of α-Fe_2O_3 nanotube/SnO_2 (FNT/S)

FNT/S was synthesized in a microwave-assisted hydrothermal process at 220 °C for 5 min with FNTs, $SnCl_4{\cdot}5H_2O$, and NaOH in 40 ml of DI water. The precipitate was centrifuged with DI water and dried.

2.3. Preparation of α-Fe_2O_3 nanotube/SnO_2/RGO (FNT/S/RGO)

FNT/S/RGO was fabricated in a two-step microwave-assisted hydrothermal process. First, an FNT solution and RGO powder were concurrently synthesized at 220 °C for 30 min, centrifuged, and dried. This synthesis was performed to improve the dispersion of the FNTs on RGO (Fig. 1) compared to that achieved through the separate synthesis of FNT and RGO [21]. Second, a powder with $SnCl_4{\cdot}5H_2O$, and NaOH in 40 ml of DI water was produced in a microwave-assisted hydrothermal process at 220 °C for 5 min.

2.4. Materials characterization

The surface morphology and structure of the FNTs, FNT/S, and FNT/S/RGO were investigated using field-emission scanning electron microscopy (FE-SEM, Hitachi S-4200 system) and high-resolution TEM (HR-TEM, JEM-ARM200F, JEOL microscope). XRD and *in situ* XRD (PANalytical) were conducted for crystal structure analysis. The specimen for HR-TEM was prepared using an ion slicer (JEOL ION SLICER, EM-09100IS) at 6 kV and a glancing angle of 4°. To define the weight ratio of FNT/S/RGO, simultaneous thermal analysis (STA, PerkinElmer, STA8000) was performed in air with a ramp rate of 10 °C min^{-1} from 25 to 1000 °C. The nitrogen adsorption isotherms and Brunauer–Emmett–Teller (BET, Micromeritcs ASAP 2020 analyzer) surface areas were examined. XPS (Thermo VG, U.K.) was conducted to characterize the bonding state and elemental distribution.

2.5. Electrochemical characterizations

FNT, FNT/S, and FNT/S/RGO were prepared using the active material (70 wt%), polyvinylidene fluoride as the binder (20 wt%), and carbon black (10 wt%) with 1-methyl-2-pyrrolidinone to characterize their electrochemical performance. The prepared FNT, FNT/S, and FNT/S/RGO electrodes were assembled into coin cells (CR2032) using Li foil and 1 M $LiPF_6$ in EC: DEC (1:1) as the electrolyte in an argon (purity: 99.999%)-filled glove box maintained at a humidity level below 6 ppm. The coin cells were rested for 4 h to stabilize the open-circuit voltage (OCV) and were subsequently cycled between 0.01 and 3 V using a battery cycler (WBCS3000) at room temperature (~298 K). The *in situ* XRD pattern of FNT/S/RGO was recorded in the 2 theta range of 26 – 38° in order to investigate main peak of Fe_2O_3 and SnO_2. The FNT/S/RGO electrode for *in situ* XRD was consisted of specialized equipment such as beryllium glass of 500 μm thick, O-ring sealed Teflon pot, and SUS packages. FNT/S/RGO electrode was assembled by same materials of Li foil, electrolyte, and separator. *In situ* EIS (BioLogic EC-Lab, VSP-300) was performed at AC frequencies from 4 MHz to 100 mHz during the charge and discharge processes.

3. Results and discussion

3.1. Materials design and structural characterization

Fig. 1 presents the synthesis procedure for the FNT, FNT/S, and FNT/S/RGO nanostructures. The TEM image and a schematic of the unique α-Fe_2O_3 nanotube (Fig. 1a) and SnO_2 nanorods (Fig. 1b and c) prepared by a microwave-assisted hydrothermal process are shown. The formation mechanism of FNT/S is explained as occurring in two steps. First, an SnO_2 nucleus nucleated on the surface of the α-Fe_2O_3 nanotubes to decrease the lattice incongruity [22]. SnO_2 nanorods have a preferred orientation of [001]. Second, SnO_2 nanorods were anisotropically formed by the dehydration of $Sn(OH)_6^{2-}$ ions as hierarchical heteronanostructures. The SnO_2 nanorod formation is related to the holding temperature control. When the holding temperature was increased from 150 to 220 °C, the length of the SnO_2 nanorods increased between the outer and inner sides of the α-Fe_2O_3 nanotubes, as shown in Fig. 1b and c.

Fig. 2 shows the nanostructure and growth behavior of the FNT, FNT/S, and FNT/S/RGO, as investigated by SEM, TEM, and energy-dispersive X-ray spectroscopy (EDS). The SEM image of the FNTs (Fig. 2a) shows their homogeneous length and their hole size. The FNT/S specimens (Fig. 2b) show the uniform growth of SnO_2 nanorods on the FNT surface, which was synthesized at 220 °C, as noted in Fig. 1. The anchored FNT/S (Fig. 2c) was homogeneously distributed on the RGO sheets, which likely facilitated the formation of anchoring of FNT/S as a heterogeneous nucleation site. The TEM image of FNT/S (Fig. 2d) shows an outer diameter (including SnO_2 nanorods) of ~230 nm and a length of ~660 nm. The TEM specimen of FNT/S was vertically milled using an ion slicer (Fig. 2g) to examine the internal structure. The SnO_2 nanorods were uniformly formed in a

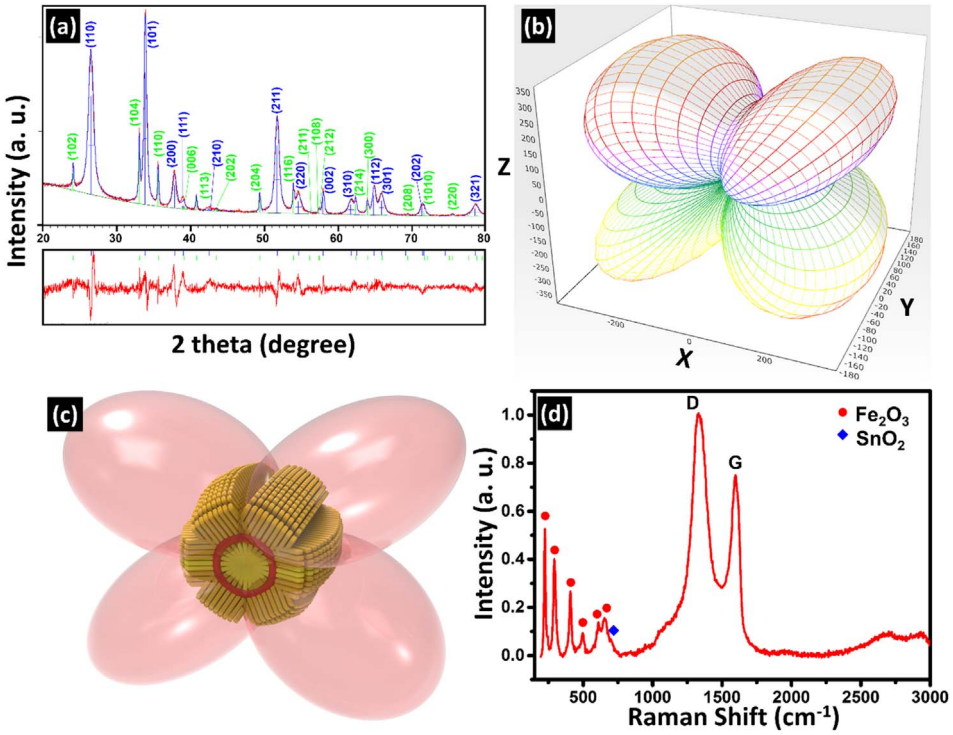

Fig. 3. Structural analysis of FNT/S/RGO: (a) the refinement plot shows the measured data in red, the total calculated profile in blue, and the background curve in green; the bottom difference plot shows the difference between calculated and observed data in red. The peak positions and intensities of the α-Fe_2O_3 phase peaks are displayed as green lines; the peaks of the SnO_2 phase are shown as blue lines. (b) Stephens model strain distribution plot based on the refined Stephens coefficients of the SnO_2 phase. (c) Schematic of the Stephens's model of the FNT/S/RGO structure. (d) Raman spectra of FNT/S/RGO.

microwave hydrothermal process at the surface and inner site of the FNTs, as shown in the cross-sectional dark-field TEM image of Fig. 2e. Moreover, the HR-TEM images (Fig. 2f) of an SnO_2 nanorod confirm its crystalline nature (lattice fringes). The fast Fourier transform (FFT) pattern (inset of Fig. 2f) was indexed to the (200) and (101) planes of the tetragonal SnO_2 phase. In addition, the growth direction of the tetragonal SnO_2 nanorod was the [001] direction, as determined from the lattice image obtained *via* HR-TEM and FFT analysis. EDS analysis revealed that the FNT/S was composed of Sn, Fe, and O, as shown in the TEM element mapping images (Fig. 2h–k). The SEM images of FNT/S reveal the optimization procedure of holding time control (Fig. S4) and temperature control for the hydrothermal process (Fig. S5) to maximize the homogeneous growth of SnO_2 nanorods on the FNT surfaces.

The XRD patterns of FNT, FNT/S, and RGO were characterized, as shown in Fig. S1. The XRD peaks of FNT were matched by α-Fe_2O_3 (a=b=5.038 Å, c=13.776 Å, JCPDS No. 01–089–0598). The sharp diffraction peaks of α-Fe_2O_3 clearly indicate that the FNTs have a crystalline structure. The diffraction peaks of FNT/S coexist with those of the tetragonal SnO_2 (a = b =4.73 Å, c =3.18 Å, JCPDS No. 01-088-0287) and the α-Fe_2O_3 phases. The RGO sheet shows no evident XRD pattern, which implies that the oxygen group of the GO sheet is substantially reduced [23].

To examine the crystal structure and growth behavior of FNT/S/RGO, Rietveld refinements were conducted, as shown in Fig. 3a. A quantitative two-phase Rietveld analysis [24,25] was performed on the XRPD data of "specimen XYZ" using α-Fe_2O_3 (a=b =5.038 Å, c =13.776 Å) and SnO_2 (a = b =4.73 Å, c =3.18 Å) as the starting model. The spherical harmonics model [26,27] was applied to better model the peak intensity because both phases exhibited several preferred orientation directions. The spherical harmonics model uses the general axis equation, as described by Bunge et al.[28] The preferred orientation correction Op (h,y) for this formulation depends on both the reflection h and the sample orientation y as follows:

$$O_p(h, y) = 1 + \sum_{L=2}^{N_L} \frac{4\Pi}{2L+1} \sum_{m=-L}^{L} \sum_{n=-L}^{L} C_L^{mn} k_L^m(h) k_L^n(y) \quad (1)$$

Typically, there are 3 (cubic) to 14 (triclinic) refinable coefficients, depending on the space-group symmetry. In addition, the SnO_2 phase shows a pronounced anisotropy of the peak full-widths at half-maxima (FWHMs). The peak half-widths slowly increase with increasing diffraction angle and depend on the crystallographic direction of the reflections. To model this directional {*hkl*} dependence of the peak half-widths, we applied the Stephens model [29]. The Stephens model is a phenomenological description of the anisotropy of the peak half-widths because of microstrain in the crystallites; it has been widely used by the Rietveld community and is implemented in many software packages. Thus, it fits the occurring variations in peak widths without explaining the physical cause. (Details of the Caglioti function are explained in the supporting text).

The use of the Stephens model finally enabled a decent fit of the data. The final refined Stephens model coefficients of the SnO_2 phase are shown in Table S5. On the basis of these coefficients, we calculated a strain distribution plot (pseudo-3D surface plot), as displayed in Fig. 3b and c. A uniform microstrain distribution resulted in a sphere. Therefore, stronger peak width anisotropy of the SnO_2 nanorod indicates a more deformed sphere. The SnO_2 nanorods should exhibit weaker structural integrity than the Fe_2O_3 nanotubes during the insertion/extraction reaction because of the microstrain induced by anisotropic grain growth.

Raman spectroscopic analysis was conducted to further confirm the composition of the FNT/S/RGO. The E_g modes of Fe_2O_3 appeared at 292, 408, and 607 cm^{-1} [30]. Moreover, a small blue-shift of the FNT/S/RGO compared to the standard Raman spectrum of Fe_2O_3 suggests an interaction between Fe_2O_3 and RGO [31]. The SnO_2 nanorod peak was assigned as 697 cm^{-1} [32]. The spectra were dominated by carbon resonances at approximately 1597 (G band) and 1339 cm^{-1} (D band), which correspond to sp^2-hybridized carbon atoms in RGO and disorder in the sp^2 carbon atoms, respectively. The I_D/I_G ratio (1.0) of the RGO sheets in FNT/S/RGO was calculated using the difference Raman spectrum (Fig. S6), where I_D indicates the nucleation site during the formation of FNT/S nanostructures.

Various carbon weight ratios (wt%) of the FNT/S/RGO were calculated using STA analysis to maximize the electrochemical perfor-

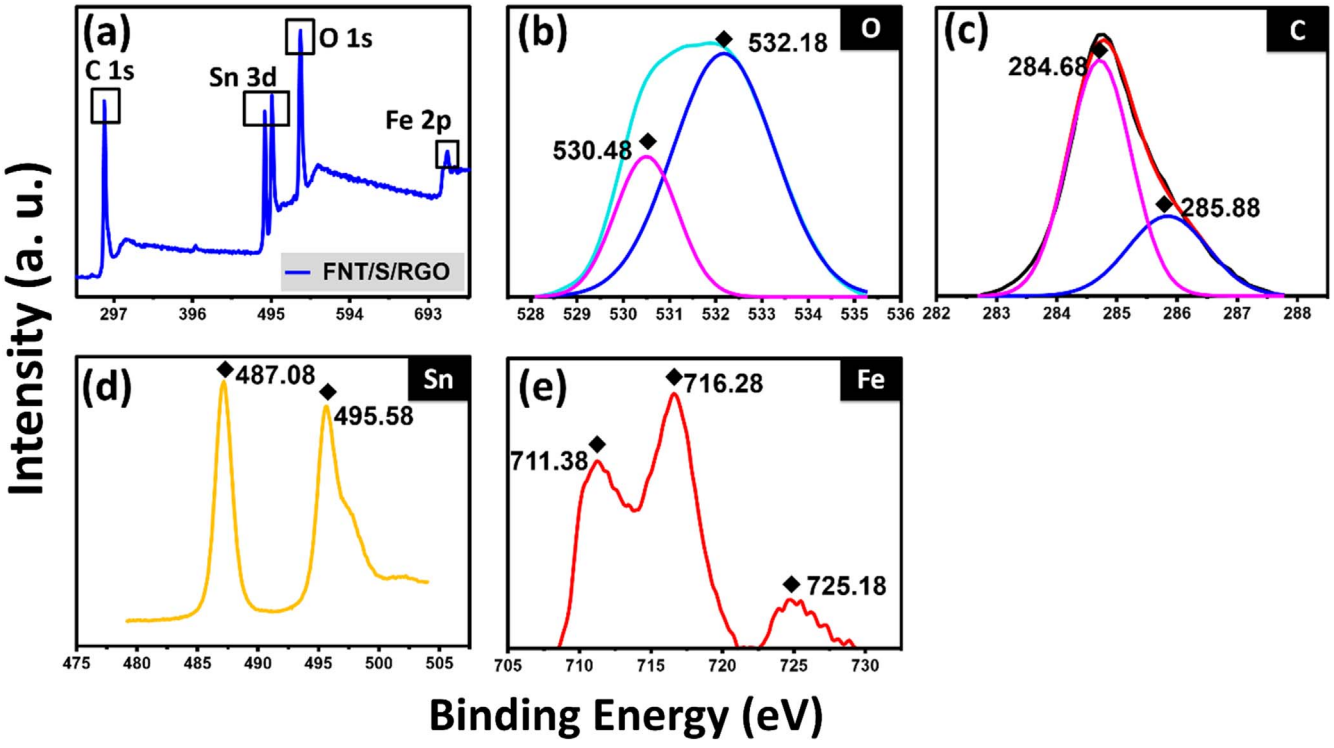

Fig. 4. X-ray photoelectron spectra: (a) wide scan of FNT/S/RGO and narrow scan of (b) O 1 s, (c) C 1 s, (d) Sn 3d, and (e) Fe 2p spectra.

mance, as shown in Fig. S7. The STA results for FNT/S/RGO in air were 27%, 34.9%, 39.8%, and 74.5%, as shown in Fig. S7a, b, c, and d, respectively. The small weight loss near 230 °C was induced by adsorbed H_2O molecules. The decomposition of RGO in FNT/S/RGO was observed at approximately 470 °C. The weight percentage of FNT/S/RGO was optimized by the presence of Fe_2O_3/SnO_2 (~60.2 wt%) and RGO (~39.8 wt%).

The BET surface areas of FNT, FNT/S, and FNT/S/RGO were revealed by the N_2 adsorption/desorption isotherms collected at 77 K. The BET specific areas for FNT, FNT/S, and FNT/S/RGO were 8.39 $m^2 g^{-1}$, 15 $m^2 g^{-1}$, and 73 $m^2 g^{-1}$, respectively, as shown in Fig. S8. Although the surface areas of FNT and FNT/S were lower than that of FNT/S/RGO, the FNT/S/RGO presented a substantially higher specific surface area because of the RGO. The substantially greater surface area of the FNT/S/RGO specimen may improve the accommodation of Li ions and enhance the contact area between the electrode and the electrolyte during the electrochemical reaction.

The elemental compositions and oxidation states of the FNT/S/RGO were further examined by XPS. The survey spectrum in Fig. 4 reveals the co-existence of O, C, Sn, and Fe. The peaks in the O 1 s spectrum (Fig. 4b) at 530.48 and 532.09 eV were attributed to O^{2-} and C–O bonding, respectively [33]. Moreover, peaks of H_2O (531.5 eV) and OH^-(533 eV) were not detected in the O 1 s spectrum, which implies that FeOOH in the FNT/S/RGO was oxidized to Fe_2O_3, consistent with the XRD results [3,33]. The C1s XPS spectrum (Fig. 4c) reveals a dominant C–C (284.68 eV) peak in the graphene planes, which indicates the reduction of oxygen groups, and a C–O peak at 285.88 eV [34]. The binding energies of Sn 3d at 487.08 and 495.58 eV were attributed to Sn $3d_{5/2}$ and Sn $3d_{3/2}$ (Fig. 4d). In Fig. 4e, the peaks at 711.38 and 725.18 eV were assigned to Fe $2p_{3/2}$ and Fe $2p_{1/2}$, respectively, which indicates the presence of Fe(III). The $Sn3p_{3/2}$ peak at approximately 716 eV provides further evidence of SnO_2 [33,35].

3.2. Electrochemical performance

The electrochemical performance of the FNT, FNT/S, FNT/S/RGO was investigated at 200 mA g^{-1} and from 0.01 to 3.0 V, as shown in Fig. 5a. The FNT exhibited an initial discharge capacity of ~793 mA h g^{-1} (see Table S6). The capacity rapidly decreased with increasing cycle number for the first 70 cycles, and the electrode maintained a capacity ~139 mA h g^{-1} at the 220th cycle, showing a capacity retention of ~17% (Table S6). The FNT electrode exhibited unsatisfactory cycle performance because FNT exhibits low electrical conductivity during the insertion/extraction. However, the initial capacity of FNT/S was ~1346 mA h g^{-1} for the first cycle (retention of 21% between the 1st and 220th cycles), which shows a more dramatic decrease in capacity and even better cycle retention than the FNT electrode, as shown in Table S6. This initial capacity decay is attributed to the higher specific surface area and conversion reaction of FNT/S of SnO_2 nanorods. The FNT/S/RGO hybrid structure delivered a first discharge capacity of ~883 mA h g^{-1} (~1871 mA h g^{-1} at 0th cycle). The discharge capacity at the 220th cycle was ~795 mA h g^{-1}, which corresponds to 90% retention between the 1st and 220th cycles, which is much higher than the retentions of both the FNT and FNT/S specimens. Remarkably, the potential *vs.* specific capacity of FNT/S/

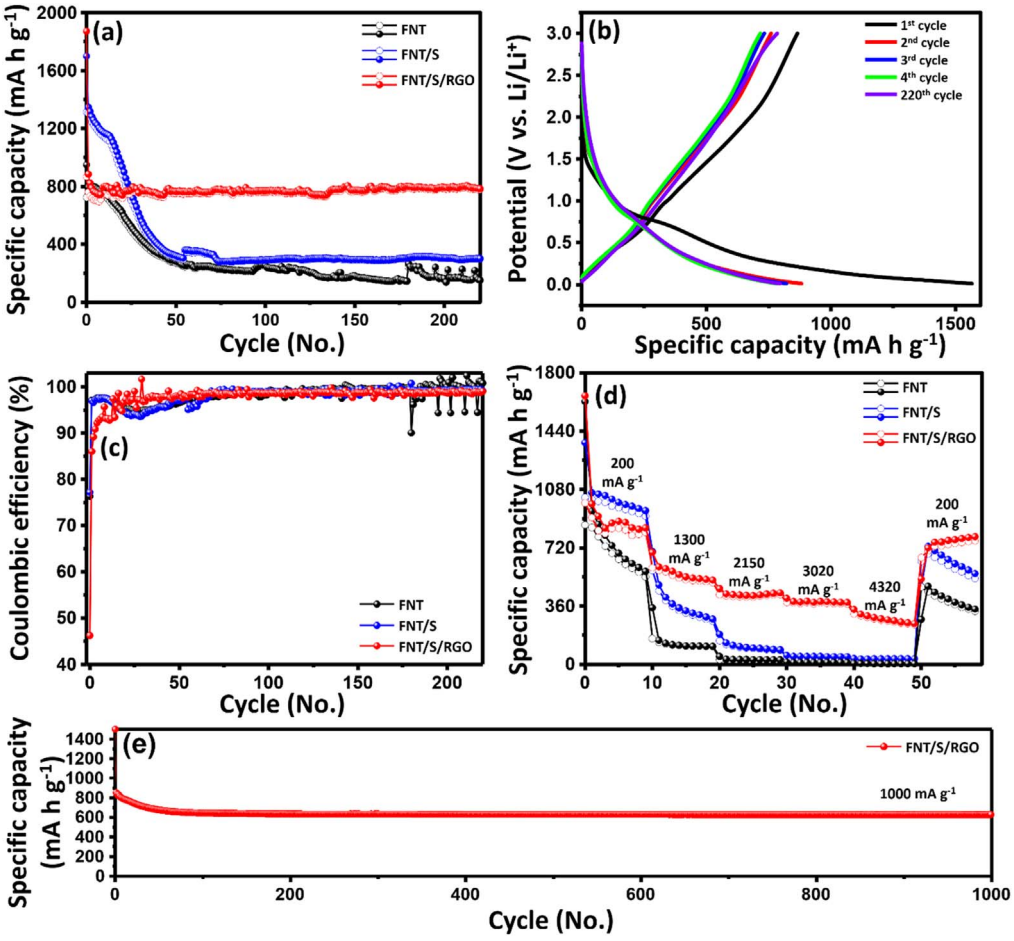

Fig. 5. Electrochemical characterization of FNT, FNT/S, and FNT/S/RGO: (a) cycle test between 0.01 and 3 V at a current density of 200 mA g^{-1}; (b) alloying/dealloying curves of the FNT/S/RGO at various cycles; (c) Coulombic efficiency of FNT, FNT/S, and FNT/S/RGO; (d) rate performance of FNT, FNT/S, and FNT/S/RGO at various current densities (200, 1300, 2150, 3020, 4320, and 200 mA g^{-1}); (e) long-term cycle test of FNT/S/RGO at a current density of 1000 mA g^{-1} for 1000 cycles.

RGO, as shown in Fig. 5b, exhibits excellent retention behavior from the 1st to 220th cycle. The coulombic efficiency (Fig. 5c) of FNT, FNT/S, and FNT/S/RGO at the 0th cycle was 76%, 77%, and 46%, respectively, which is attributed to electrolyte decomposition and SEI formation on the electrode surface [36,37]. Although the lowest coulombic efficiency of FNT/S/RGO during the 0th cycle was a consequence of the high specific surface area induced by SEI, the coulombic efficiency of FNT/S/RGO was progressively restored after the 13th cycle.

The rate capability of FNT, FNT/S, and FNT/S/RGO as anodes was confirmed at various current densities (200, 1300, 2150, 3020, 4320, and 200 mA g^{-1}), as shown in Fig. 5d. The rate capability of the FNT electrode showed poor performance: it substantially decreased from 200 mA g^{-1} in the 10th cycle to 4320 mA g^{-1} in the 50th cycle (retention: 59%; 1st step – last step), as shown in Table S7. The FNT/S electrode exhibited more stable rate capability than FNT and exhibited a capacity retention of 58.8% (1st step – last step). The FNT/S/RGO electrode exhibited a much higher rate capability than FNT and FNT/S at all rate steps with better capacity retention (93.4%). From these results, FNT/S/RGO has the highest electrochemical performance in terms of the cycle durability and high rate (4320 mA g^{-1}) in the cycle test. The long-term cyclability of the FNT/S/RGO electrode was investigated for 1000 cycles at a current density of 1000 mA g^{-1} and is shown in Fig. 5e. The superior reversible capacity was 854 mA h g^{-1} in the first cycle with a low capacity fade to 690 mA h g^{-1} after 1000 cycles. The superior cycle retention and rate capability of FNT/S/RGO is clearly attributable to the hybrid structure of RGO, α-Fe_2O_3, and SnO_2, which is explained as follows: The RGO provides an enhanced conductive network and volume expansion resistance as a consequence of its free space; Li ions have abundant space because of the functional groups of RGO sheets; [38] and the Li ions have a short diffusion path as a consequence of the SnO_2 nanorod and α-Fe_2O_3 nanotube structure.

To confirm the electrochemical reactions of FNT/S/RGO during Li insertion/extraction, cyclic voltammetry (CV) was conducted at a scan rate of 0.1 mV s^{-1} for 8 cycles. As shown in Fig. 6a, in the first cycle, α-Fe_2O_3 and SnO_2 reacted with Li ions coexisted during the insertion/extraction. The cathodic peaks at 1.49, 0.88, and 0.6 V in the first cycle

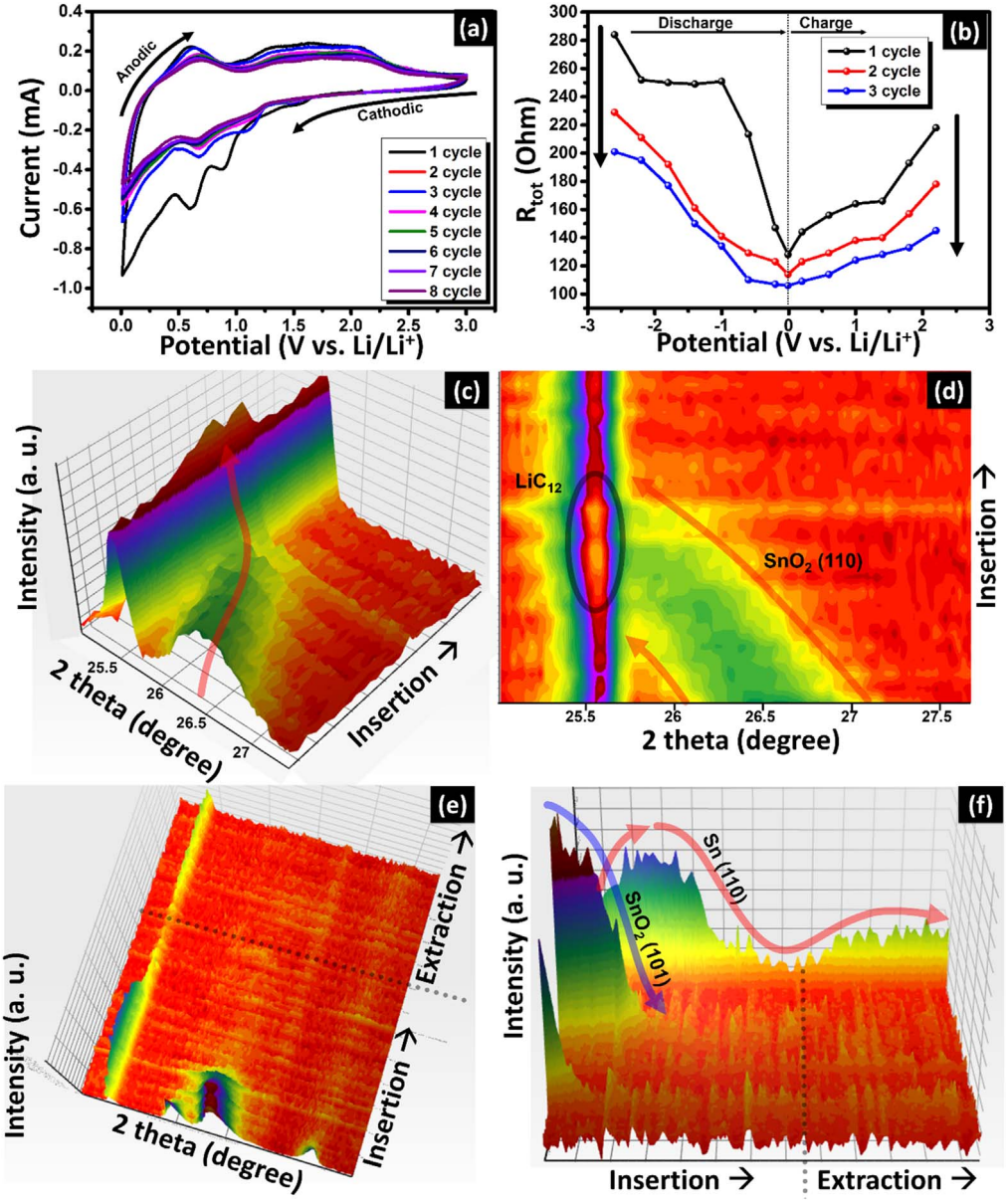

Fig. 6. (a) Cyclic voltammograms of FNT/S/RGO at a scan rate of 0.1 mV s^{-1} for 8 cycles; (b) *in situ* EIS data for FNT/S/RGO from OCV (~2.6 V) to 0.01 V for 3 cycles; selected *in situ* XRD patterns of FNT/S/RGO in the 2-theta range of (c) 3D plot of 25–27.5°, (d) top view of 25–27.5°, (e) 3D plot of 31.5–36.5°, and top view of 31.5–36.5°.

are attributed to the sequential reaction of Fe^{3+} to Fe^{2+} and Fe°, respectively, in conjunction with SEI layer formation on the surface of the active materials [36,39,40]. In the cathodic scan, the peak at 1.09 V is assigned to the SnO_2 reduction to Sn in conjunction with Li_2O formation, as given in Eq. (5) [41]. The peak at approximately 0.014 V is attributed to the LiC_6 reaction of RGO in Eq. (7) [42]. In the anodic scan, the peaks of 0.60, 1.3, and 2.0 V are ascribed to the process of Li-ion extraction from the Li_xSn phase (Eq. (6)), [43] the reduction reaction of SnO_2 to Sn, and the oxidation of Fe° to Fe^{3+}(Eq. (8)), respectively [36].

$$SnO_2+4Li^++4e^-\leftrightarrow 2Li_2O+Sn \quad (5)$$

$$Sn+xLi^++xe^-\leftrightarrow Li_xSn \quad (6)$$

$$C_6\ (RGO)+Li^++e^-\leftrightarrow LiC_6 \quad (7)$$

$$\alpha\text{-}Fe_2O_3+6Li^++6e^-\leftrightarrow 3Li_2O+2Fe \quad (8)$$

The charge/discharge characteristics of the FNT/S/RGO specimen exhibited good overlap in each cycle, which implies better capacity retention with increasing number of cycles than the FNT and FNT/S specimens, as shown in Fig. S11.

FNT/S/RGO was investigated with *in situ* EIS to define the correlations between the electrochemical performance and the hybrid structure of FNT/S/RGO during the insertion/extraction reaction. The *in situ* EIS of FNT/S/RGO was measured from the open-circuit voltage (OCV, ~2.6 V) to 0.01 V for 3 cycles. Figs. S12, S13, and S14 show the measured potentials on the voltage *vs*. capacity plot, Nyquist plots, and the total resistance (R_{tot}) values, respectively. The R_{tot} was 284 Ω at the OCV of the 0th cycle and decreased to 125 Ω according to the insertion of Li ions during the discharge step. Subsequently, R_{tot} in the charge step reversibly increased to 218 Ω. The R_{tot} of the 1st and 2nd cycles also followed the electrochemical behavior of the 0th cycle. Finally, the R_{tot} of FNT/S/RGO decreased from 284 Ω in the 0th cycle to 145 Ω in the 2nd cycle, which suggests that the electrical conductivity of FNT/S/RGO was enhanced by the increase in Li-ion concentration in the electrode [44]. The steep slope of the Warburg tail during all cycles was kinetically assigned to rapid Li-ion diffusion from the electrolyte to the electrode surface.

To further examine the phase transition of FNT/S/RGO during the insertion/extraction, *in situ* XRD was conducted for 1 cycle in the potential range from 0.01 to 3.0 V. The overall XRD pattern clearly indicates changes in the peak intensity, phase transitions, and mainly the diffraction ranges 25–27.5° and 31.5–36.5°, as shown in Fig. 6c–f. The diffraction peaks of SnO_2 (110) at 26.5° gradually shifted to low angles at 25.5° 2θ during the insertion process, which is related to the lattice expansion according to the increasing Li concentration, as shown in Fig. 6c and d. The XRD peak intensity of LiC_{12} at 25.5° 2θ (Fig. 6d) slightly increased during the extinction of the SnO_2 (110) peak, which might maximize the LiC_{12} reaction and recover to the previous intensity after the insertion process. In the case of the diffraction range from 31.5 to 36.5° 2θ, the diffraction peak of SnO_2 (101) disappeared during the insertion process. However, the Sn (110) metal peak appeared, coinciding with the extinction of the SnO_2 (101) peak, as shown in Fig. 6e and f. Hence, the SnO_2 phase was converted to the Sn metal phase during the insertion reaction in the 1st cycle. These *in situ* XRD results show that the SnO_2 conversion process during insertion/extraction can improve the electrical conductivity and electrochemical performance, consistent with the *in situ* EIS results.

Ex situ TEM (Fig. 7a–g) after the cycling of FNT/S/RGO and elemental mapping (Figs. S9 and S10) was performed. The surface of FNT/S at 1 V in the first cycle discharge became an amorphous phase,

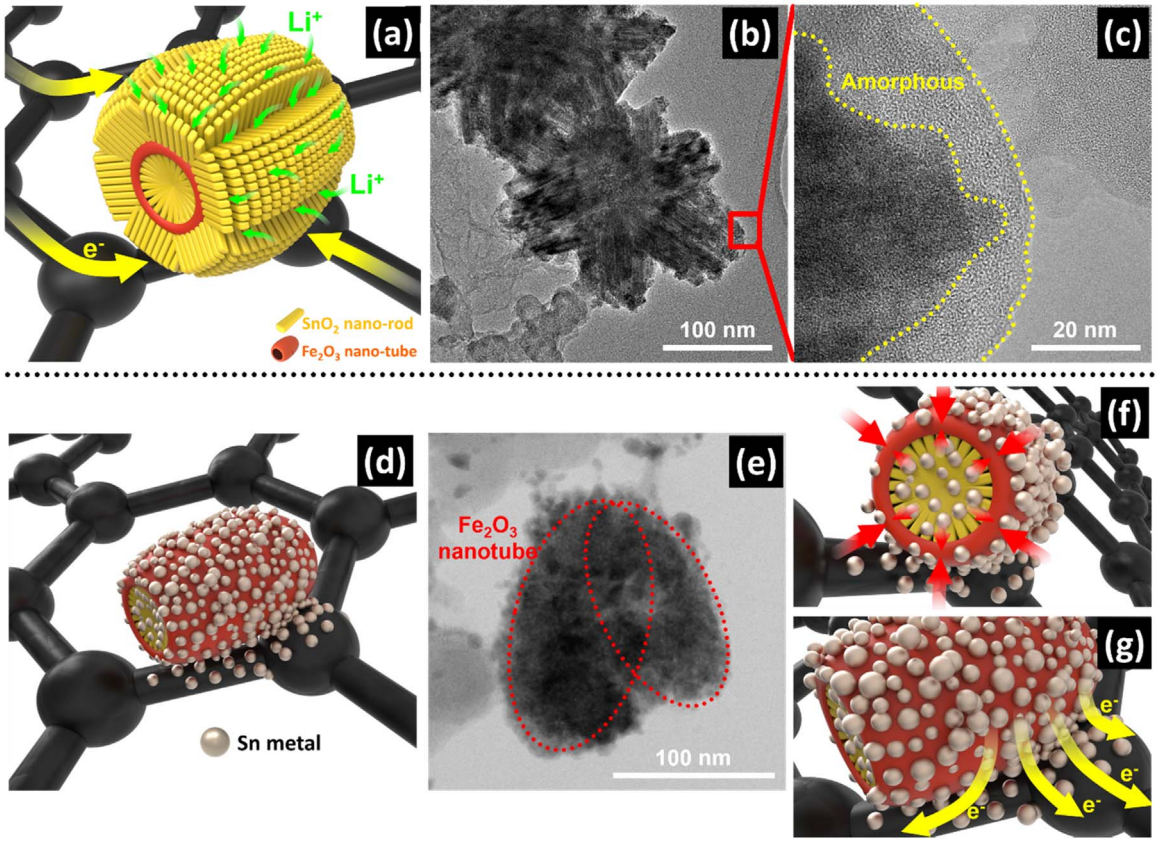

Fig. 7. (a) Schematic of the alloying/dealloying behavior of FNT/S/RGO; (b) *ex situ* TEM image of FNT/S/RGO after the first alloying step at 1 V; (c) enlarged image of boxed area from (b); (d) schematic of FNT/S/RGO; (e) *ex situ* TEM image of FNT/S/RGO after 3 cycles; (f) schematic of the volume expansion of FNT/S/RGO being prevented during the alloying/dealloying process; (g) schematic of the improved electrical conductivity of FNT/S/RGO after the conversion of SnO_2 to Sn metal.

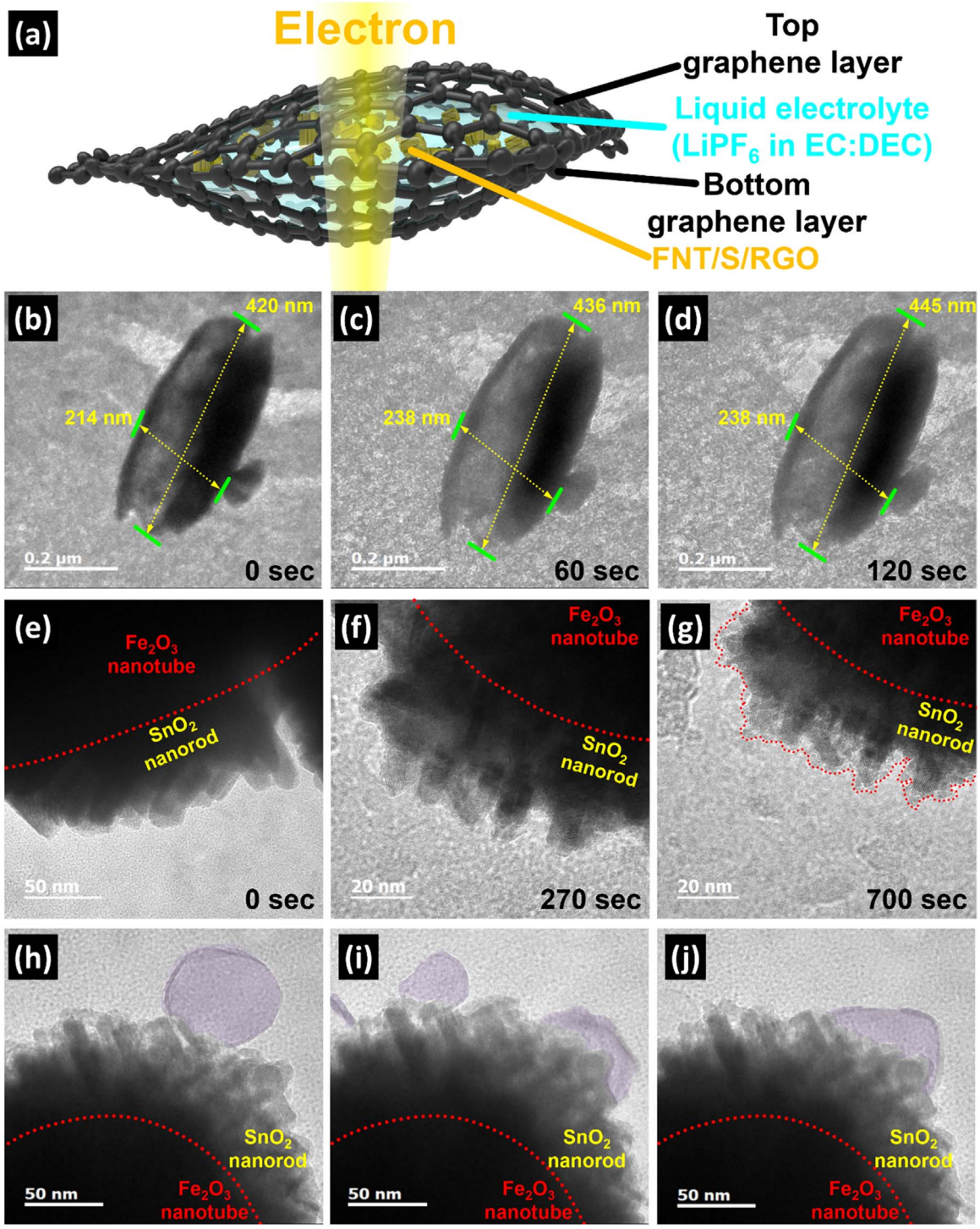

Fig. 8. (a) Schematic of the *in situ* TEM of FNT/S/RGO encapsulated by two graphene sheets. FNT/S/RGO was immersed in the liquid electrolyte ($LiPF_6$ in EC: DEC =50:50 vol). (b)–(d) *In situ* TEM of FNT; (e)–(g) *in situ* TEM of FNT/S/RGO; (h)–(j) SEI layer observation of FNT/S/RGO.

and the insertion of Li ions into the FNT/S surface was confirmed, as shown in Fig. 7a, b and c. The elemental mapping image in Fig. 7b shows that FNT/S/RGO after the cycling test consisted of the carbon of RGO and the electrolyte, fluorine of $LiPF_6$, oxygen of SnO_2 and Fe_2O_3, iron of the Fe_2O_3 nanotubes, and Sn of the SnO_2 nanorods (Fig. S9). The charge/discharge mechanism of the multi-metal oxide electrode of FNT/S/RGO confirms that the part of the SnO_2 nanorod under greater strain preferentially collapses with an increase in the amount of inserted Li ions, which results in the strain distribution observed in the 3D Stephens model (Fig. 3b). After 3 cycles, FNT was structurally intact and its surface was covered with Sn metal (Fig. 7e and elemental mapping image in Fig. S10), consistent with the *in situ* EIS and *in situ* XRD results.

The FNTs were also investigated using real-time *in situ* TEM observations, as shown in Fig. 8a–j. Fig. 8a schematically illustrates the *in situ* TEM observations using a stack of two graphene cells, as reported elsewhere [20]. Although FNT exhibited a dynamic reaction with Li (see supporting information for Movie 1), FNT exhibited good resistance to volume expansion with increasing reaction time, as shown in Fig. 7e. The SnO_2 nanorods in Fig. 8e–g was lithiated within 700 s;

its crystal structure collapsed and was converted to an amorphous structure with increasing lithiation state (movie 2). This result is also consistent with the *ex situ* TEM results and the higher stress of SnO_2 nanorods, as shown in the 3D Stephens model. The SnO_2 nanorods exhibit weak resistance to volume changes, which results in enhanced electrical conductivity as a sacrificial material, excellent cyclability and high rate capability. The formation of an SEI layer on the FNT/S/RGO surface, as shown in Fig. 8h–j (Movie 3), was much better than that on FNT, which is related to the higher specific surface area and greater irreversible capacity of FNT/S/RGO, as shown in Fig. 5a. These results show that the initial irreversible capacity of the multi-metal oxide electrode is associated with the irreversible phase conversion and strain distribution of the 3D Stephens model.

Supplementary material related to this article can be found online at http://dx.doi.org/10.1016/j.nanoen.2016.12.058.

4. Conclusion

Starting with an SnO_2 nanorod array as the sacrificial material for the electrical conductivity, we successfully fabricated FNT/S/RGO an anode *via* a microwave-assisted hydrothermal process without hard templating. The FNT/S/RGO exhibited substantially better electrochemical properties than many SnO_2/Fe_2O_3 nanostructured anodes, which we attributed to the short diffusion distance and improved electrical conductivity resulting from the synergistic effect between SnO_2 and Fe_2O_3. Moreover, the RGO sheets have better electrical conductivity for faster electrochemical kinetics and an elastic buffer effect to prevent the expansion of SnO_2 and Fe_2O_3 during the insertion/extraction reaction. Consequently, this hybrid structure of FNT/S/RGO shows an outstandingly long cycle life (690 mA h g^{-1} after 1000 cycles) at high rates (1000 mA g^{-1}); it can also deliver a specific capacity of 795 mA h g^{-1} after 220 cycles at 280 mA g^{-1} with good capacity retention (as high as 90%). Moreover, the lithiation behavior and electrochemical enhancements of FNT/S/RGO were observed in various *in situ* analyses and in the 3D strain distribution of the Stephens model. The highly functional 3D nanostructures of the FNT/S/RGO composite are composed of naturally abundant materials, inexpensive, amenable to mass production, and exhibit a high energy density, which should impart them with a wide range of applications in, for example, Li- and Na-ion batteries, supercapacitors, photocatalysts, water-splitting catalysts, and gas sensors.

Acknowledgements

This study was supported by the National Strategic R & D Program for Industrial Technology (10043868), which was funded by the Ministry of Trade, Industry and Energy (MOTIE).

Appendix A. Supplementary material

Supplementary data associated with this article can be found in the online version at http://dx.doi.org/10.1016/j.nanoen.2016.12.058.

References

[1] Z.-S. Wu, G. Zhou, L.-C. Yin, W. Ren, F. Li, H.-M. Cheng, Nano Energy 1 (2012) 107–131.
[2] M.V. Reddy, G.V. Subba Rao, B.V.R. Chowdari, Chem. Rev. 113 (2013) 5364–5457.
[3] Y. Yang, X. Fan, G. Casillas, Z. Peng, G. Ruan, G. Wang, M.J. Yacaman, J.M. Tour, ACS Nano 8 (2014) 3939–3946.
[4] Y.-M. Lin, P.R. Abel, A. Heller, C.B. Mullins, J. Phys. Chem. Lett. 2 (2011) 2885–2891.
[5] W. Zeng, F. Zheng, R. Li, Y. Zhan, Y. Li, J. Liu, Nanoscale 4 (2012) 2760–2765.
[6] J.B. Fei, Y. Cui, X.H. Yan, W. Qi, Y. Yang, K.W. Wang, Q. He, J.B. Li, Adv. Mater. 20 (2008) 452–456.
[7] G. Xia, N. Li, D. Li, R. Liu, C. Wang, Q. Li, X. Lü, J.S. Spendelow, J. Zhang, G. Wu, ACS Appl. Mater. Interfaces 5 (2013) 8607–8614.
[8] J.S. Chen, C.M. Li, W.W. Zhou, Q.Y. Yan, L.A. Archer, X.W. Lou, Nanoscale 1 (2009) 280–285.
[9] W. Zhou, C. Cheng, J. Liu, Y.Y. Tay, J. Jiang, X. Jia, J. Zhang, H. Gong, H.H. Hng, T. Yu, H.J. Fan, Adv. Funct. Mater. 21 (2011) 2439–2445.
[10] S. Xu, C.M. Hessel, H. Ren, R. Yu, Q. Jin, M. Yang, H. Zhao, D. Wang, Energy Environ. Sci. 7 (2014) 632–637.
[11] W. Zhou, Y.Y. Tay, X. Jia, D.Y. Yau Wai, J. Jiang, H.H. Hoon, T. Yu, Nanoscale 4 (2012) 4459–4463.
[12] D.T. Ngo, H.T.T. Le, C. Kim, J.-Y. Lee, J.G. Fisher, I.-D. Kim, C.-J. Park, Energy Environ. Sci. 8 (2015) 3577.
[13] D. Kong, H. He, Q. Song, B. Wang, W. Lv, Q.-H. Yang, L. Zhi, Energy Environ. Sci. 7 (2014) 3320–3325.
[14] X. Liu, J. Zhang, W. Si, L. Xi, B. Eichler, C. Yan, O.G. Schmidt, ACS Nano 9 (2015) 1198–1205.
[15] Y. Chen, X. Li, X. Zhou, H. Yao, H. Huang, Y.-W. Mai, L. Zhou, Energy Environ. Sci. 7 (2014) 2689.
[16] S.J. Kim, S.-Y. Noh, A. Kargar, D. Wang, G.W. Graham, X. Pan, Chem. Commun. 50 (2014) 9932–9935.
[17] X.H. Liu, Y. Liu, A. Kushima, S. Zhang, T. Zhu, J. Li, J.Y. Huang, Adv. Energy Mater. 2 (2012) 722–741.
[18] M.T. McDowell, S. Woo Lee, C. Wang, Y. Cui, Nano Energy 1 (2012) 401–410.
[19] J.Y. Cheong, J.H. Chang, H.K. Seo, J.M. Yuk, J.W. Shin, J.Y. Lee, I.-D. Kim, Nano Energy 25 (2016) 154–160.
[20] J.M. Yuk, J. Park, P. Ercius, K. Kim, D.J. Hellebusch, M.F. Crommie, J.Y. Lee, A. Zettl, A.P. Alivisatos, Science 336 (2012) 61–64.
[21] K.S. Lee, S. Park, W. Lee, Y.S. Yoon, ACS Appl. Mater. Interfaces 8 (2016) 2027–2034.
[22] D.-F. Zhang, L.-D. Sun, C.-J. Jia, Z.-G. Yan, L.-P. You, C.-H. Yan, J. Am. Chem. Soc. 127 (2005) 13492–13493.
[23] D. Chen, L. Li, L. Guo, Nanotechnology 22 (2011) 325601.
[24] H. Rietveld, J. Appl. Crystallogr. 2 (1969) 65–71.
[25] R.J. Hill, C.J. Howard, J. Appl. Crystallogr. 20 (1987) 467–474.
[26] M. Jarvinen, J. Appl. Crystallogr. 26 (1993) 525–531.
[27] R. Von, J. Appl. Crystallogr. 30 (1997) 517–525.
[28] H.J. Bunge, Texture Analysis in Materials Science : Mathematical Methods, H.-J. Bunge,; translated by Peter R. Morris, Butterworths, London, Boston, 1982.
[29] P. Stephens, J. Appl. Crystallogr. 32 (1999) 281–289.
[30] D.L.A. de Faria, S. Venâncio Silva, M.T. de Oliveira, J. Raman Spectrosc. 28 (1997) 873–878.
[31] X. Teng, D. Black, N.J. Watkins, Y. Gao, H. Yang, Nano Lett. 3 (2003) 261–264.
[32] L. Shi, Y. Xu, Q. Li, Nanoscale 2 (2010) 2104–2108.
[33] Y. Luo, J. Luo, J. Jiang, W. Zhou, H. Yang, X. Qi, H. Zhang, H.J. Fan, D.Y.W. Yu, C.M. Li, T. Yu, Energy Environ. Sci. 5 (2012) 6559–6566.
[34] S. Stankovich, D.A. Dikin, R.D. Piner, K.A. Kohlhaas, A. Kleinhammes, Y. Jia, Y. Wu, S.T. Nguyen, R.S. Ruoff, Carbon 45 (2007) 1558–1565.
[35] Y.Y. Fu, R.M. Wang, J. Xu, J. Chen, Y. Yan, A.V. Narlikar, H. Zhang, Chem. Phys. Lett. 379 (2003) 373–379.
[36] G. Zhou, D.-W. Wang, P.-X. Hou, W. Li, N. Li, C. Liu, F. Li, H.-M. Cheng, J. Mater. Chem. 22 (2012) 17942–17946.
[37] P. Poizot, S. Laruelle, S. Grugeon, L. Dupont, J.M. Tarascon, Nature 407 (2000) 496–499.
[38] D. Pan, S. Wang, B. Zhao, M. Wu, H. Zhang, Y. Wang, Z. Jiao, Chem. Mater. 21 (2009) 3136–3142.
[39] Y. Zou, J. Kan, Y. Wang, J. Phys. Chem. C 115 (2011) 20747–20753.
[40] Y. Dong, K.C. Yung, R. Ma, X. Yang, Y.-S. Chui, J.-M. Lee, J.A. Zapien, Carbon 86 (2015) 310–317.
[41] R. Li, X. Ren, F. Zhang, C. Du, J. Liu, Chem. Commun. 48 (2012) 5010–5012.
[42] J. Yao, X. Shen, B. Wang, H. Liu, G. Wang, Electrochem. Commun. 11 (2009) 1849–1852.
[43] X. Wang, X. Zhou, K. Yao, J. Zhang, Z. Liu, Carbon 49 (2011) 133–139.
[44] S. Yang, H. Song, X. Chen, Electrochem. Commun. 8 (2006) 137–142.

Kangsoo Lee is currently a Ph.D. candidate in the Department of Materials Science and Engineering at Yonsei University, Seoul, Korea. His research is focused on the fabrication and investigation of nanostructured and thin film anode for high performance Li-ion batteries.

Seoyoon Shin is now pursuing a master course in the Department of Nanoscience and Technology in Gachon University, Gyonggi-Do, Korea. Her research interest mainly focuses on the fabrication of solid state electrolyte for all solid state batteries.

Thomas Degen is currently working in the development department of PANalytical B.V., Almelo the Netherlands. He gained his Ph.D. working in the field of solid state chemistry at the Institute of Inorganic Chemistry, University of Bonn, Germany. His research is mainly focused on algorithms and computing in the field of X-ray powder diffraction.

Wooyoung Lee is a Professor of Department of Materials Science and Engineering at Yonsei University in Korea. He received a BS and MS degree in metallurgical engineering from the Yonsei University. He received a Ph.D. degree in Physics from University of Cambridge, England. In recent years, his research interests have centered on thermo-electric materials and devices, various chemical sensors, quantum transports in nano-devices and novel permanent magnets.

Young Soo Yoon is Professor in Chemical Engineering at Gachon University. His current research interests are (i) all-solid Li-based secondary battery materials and systems, (ii) anode and cathode materials and systems for DMFCs, and (iii) process and device development based on two-dimensional structures. He has expertise in the thin film process and measurement and synthesis of nanotailored ceramic–metal composite powder for electrodes and solid electrolytes of Li batteries and catalysts for fuel cells.